Multifunctional GelMA/CeO_2-TA Composite Hydrogel for Wound Microenvironment Regulation and Accelerated Wound Healing

Jia Xu[1]

Received May 21, 2026
Accepted October 15, 2026
Electronic access November 15, 2026

Skin wound healing is often delayed by bacterial infection, excessive reactive oxygen species (ROS), and persistent inflammation. Developing multifunctional biomaterials that can regulate these pathological factors remains highly desirable for advanced wound care. Here, we designed a photocrosslinked GelMA hydrogel incorporating cerium oxide nanoparticles (CeO_2 NPs) and tannic acid (TA), termed Gel@CeO_2-TA, to construct a favorable wound microenvironment. The incorporation of CeO_2 NPs was confirmed by transmission electron microscopy, X-ray diffraction, X-ray photoelectron spectroscopy, dynamic light scattering, and zeta-potential analysis. The composite hydrogel maintained rapid photocuring ability and a porous architecture, while exhibiting enhanced compressive properties, tissue adhesion, and interfacial toughness compared with GelMA alone. Gel@CeO_2-TA demonstrated strong ROS-scavenging capacity, removing approximately 95% of DPPH radicals, 96% of hydroxyl radicals, and 95% of H_2O_2. It also showed effective antibacterial activity against *S.aureus* and *E.coli*, with inhibition rates of approximately 95% and 92%, respectively. In a full-thickness skin wound model, Gel@CeO_2-TA significantly accelerated wound closure, reducing the residual wound area to approximately 22% on day 10, compared with 45% in the untreated control and 32% with a commercial dressing. Histological analysis revealed enhanced re-epithelialization and collagen organization. Immunofluorescence staining showed decreased CD86 expression and increased CD206 expression, suggesting a shift toward a pro-repair macrophage phenotype. No obvious histopathological abnormalities were observed in major organs. Overall, Gel@CeO_2-TA integrates antioxidant, antibacterial, adhesive, and immunomodulatory functions, providing a promising platform for multifunctional wound repair.

Keywords: skin wound; GelMA; hydrogel; tannic acid; cerium oxide

Introduction

Skin repair proceeds through overlapping hemostatic, inflammatory, proliferative, and remodeling phases. Persistent infection, oxidative stress, and unresolved inflammation can disrupt these coordinated stages and delay closure[1-5]. Hydrogels are attractive wound dressings because their hydrated three-dimensional networks can maintain a moist interface and support diffusion of nutrients and metabolites[6,7]. Gelatin methacryloyl (GelMA) is widely used because it is photocrosslinkable, biocompatible, and cell adhesive. However, pristine GelMA has limited intrinsic antioxidant and antibacterial activity, and its mechanical and tissue-adhesive performance may be insufficient for dynamic wound surfaces[8-10].

TA is a natural polyphenol with abundant phenolic hydroxyl groups. It can participate in hydrogen bonding and interfacial interactions, while also providing radical-scavenging and antibacterial functions[11-13]. Ceria is redox active because surface cerium can reversibly cycle between Ce^{3+} and Ce^{4+} states. The accessible surface fraction, oxygen-vacancy density, and Ce^{3+}/Ce^{4+} balance are strongly size dependent[14-17]. These features provide a mechanistic basis for the antioxidant behavior of nanoceria. Prior studies have shown that nanoscale CeO_2 can scavenge ROS, modulate inflammation, and support tissue repair[18,19]. TA-associated ceria systems are particularly relevant because TA can alter surface chemistry, dispersion, and redox behavior. Direct examples include TA-conjugated ceria nanoparticles, TA-Ce nanoenzymes, and tannin-bridged CeO_2 wound materials[20-23].

Metal-phenolic nanozyme systems also illustrate how polyphenol coordination can be used to tune local ROS chemistry. CuTA platforms have been used for microenvironment-responsive ROS regulation and antimicrobial therapy, while AuNP-TA and TA-Ce systems have shown combined antioxidant and anti-inflammatory effects in other disease models[11-13,22,24]. Importantly, the same metal-polyphenol design principle can produce either ROS-scavenging or ROS-generating behavior depending on the metal center, oxidation state, and surrounding microenvironment[13]. Therefore, the catalytic mechanism of each material must be interpreted from its own composition and supporting assays rather than from

[1] *Beijing 101 High School, Beijing, China*

© The National High School Journal of Science 2026

the metal-polyphenol label alone.

In this study, we developed a multifunctional GelMA hydrogel incorporating cerium oxide nanoparticles (CeO_2 NPs) and tannic acid (TA), termed Gel@CeO_2-TA. Gel, Gel@CeO_2, and Gel@TA were included as control groups to clarify the contribution of each component. The physicochemical properties, degradation behavior, antioxidant and antibacterial activities, and tissue adhesion of the hydrogels were systematically evaluated. A full-thickness skin wound model was further used to assess wound closure, tissue regeneration, macrophage polarization, and major-organ biosafety. We hypothesized that the combined incorporation of CeO_2 and TA could strengthen the GelMA network and improve ROS scavenging, antibacterial activity, and inflammatory regulation, thereby creating a favorable microenvironment for wound repair.

Materials and Methods

Synthesis of Methacrylated Gelatin (GelMA)

GelMA was synthesized following an established protocol. Briefly, 25 g of fish skin-derived gelatin was dissolved in 250 mL of ultrapure water at 50 °C. Methacrylic anhydride (MA, 20 mL, all chemical reagents were purchased directly from Aladdin and used as received, without any further purification) was added dropwise under vigorous stirring for 3 h at 50 °C. The mixture was dialyzed (10 kDa MWCO) against ultrapure water for 4 days to remove unreacted MA, lyophilized, and stored at 4 °C protected from light.

Synthesis of Cerium Oxide Nanoparticles (CeO_2 NPs)

CeO_2 NPs were prepared via hydrothermal precipitation. Cerium nitrate hexahydrate (0.43 g) was dissolved in 100 mL of ultrapure water and stirred for 1 h. NaOH solution (1 mol/L, 10 mL) was added dropwise under continuous stirring for 5 h to form a precipitate. The product was centrifuged (5000 rpm, 20 min), washed with ethanol and water, dried at 80 °C, ground into powder, and calcined at 500 °C for 8 h.

Preparation of Hydrogel Formulations

Four hydrogel formulations were prepared with the same GelMA and photoinitiator concentrations: Gel, Gel@CeO_2, Gel@TA, and Gel@CeO_2-TA. Sterile 0.01 M PBS (pH 7.4) was used as the precursor solvent. GelMA was first dissolved at 37 °C in a water bath, and the precursor pH was adjusted to 7.4. For each batch, the final precursor volume was 10 mL and the GelMA concentration was 10 wt.%. Gel contained 10 wt.% GelMA and 10 mg mL^{-1} LAP. Gel@CeO_2 additionally contained 4 μg mL^{-1} CeO_2 NPs. Gel@TA contained 39.5 μg mL^{-1} TA. Gel@CeO_2-TA contained both 4 μg mL^{-1} CeO_2 NPs and 39.5 μg mL^{-1} TA. The components were added in a fixed order: GelMA, pre-sonicated CeO_2 NP stock, TA stock, and finally LAP. The mixture was gently stirred for 5 min after each addition, followed by probe sonication at 300 W for three 10 s cycles to reduce particle aggregation. The resulting precursor remained visually homogeneous, with no obvious GelMA precipitation or CeO_2 sedimentation within 60 min before curing. The precursor was then photocrosslinked under 405 nm light for 60 s.

Physicochemical Characterization

Gelatin and GelMA were analyzed by ^1H NMR in D_2O and by ATR-FTIR. The GelMA spectrum was reprocessed with attention to the methacryloyl regions near 5.4-6.1 ppm and the methyl resonance near 1.9 ppm. CeO_2 morphology was evaluated by transmission electron microscopy (TEM) with elemental mapping. Hydrodynamic size and zeta potential were measured by dynamic light scattering. Crystal structure was analyzed by X-ray diffraction (XRD), and cerium oxidation states were assessed by X-ray photoelectron spectroscopy (XPS), including Ce 3d peak deconvolution.

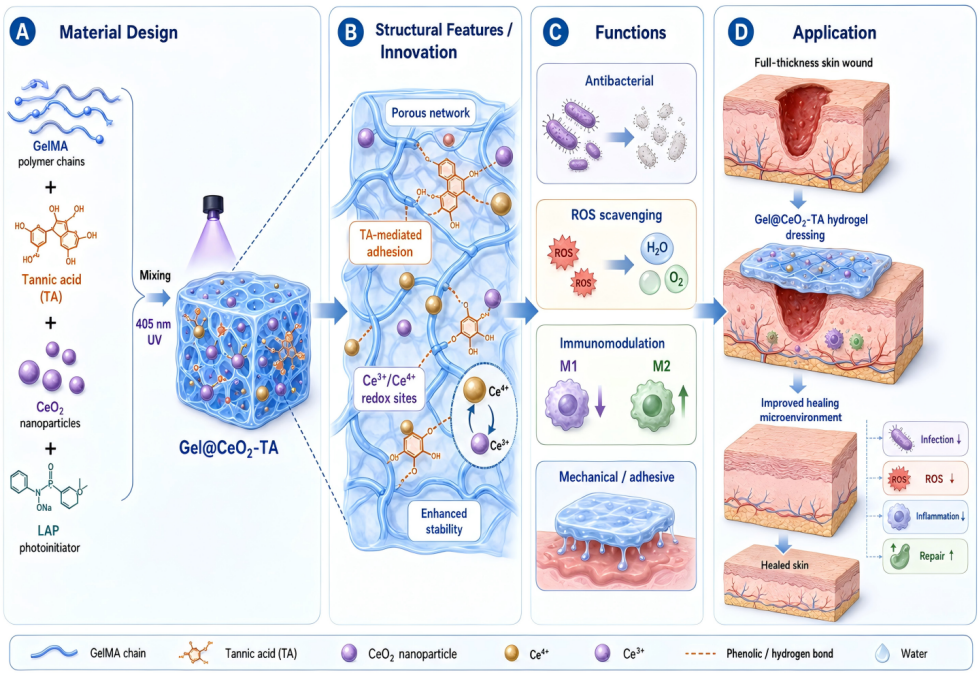
Release and Degradation

The cumulative release of the CeO_2-containing phase from Gel@CeO_2-TA was monitored over 48 h by measuring the cerium concentration in the collected release medium using inductively coupled plasma optical emission spectrometry (ICP-OES). For degradation testing, hydrogel samples were incubated in PBS at 37 °C. At predetermined time points, samples were collected, washed, dried to constant mass, and weighed. Residual mass was calculated as $W_t/W_0 \times 100\%$, where W_0 and W_t are the initial and remaining dry masses.

Rheological and Mechanical Testing

Rheological behavior was measured using a rheometer equipped with a UV curing module at 25 °C, 1 Hz, and 1% strain. Mechanical properties were measured using a universal mechanical tester (SANS, CMT2503) equipped with a 20 N load cell. For tensile testing, dumbbell-shaped hydrogel samples were prepared with a gauge length of 30 mm, a width of 5 mm, and a thickness of 2 mm. The samples were tested without additional pretreatment. Both ends were fixed in the upper and lower grips. Tensile testing was performed at 1 mm min^{-1} until complete fracture. Elongation at break was determined at the failure point. Tensile toughness was calculated by integrating the entire stress-strain curve from the start of loading to fracture. For compression testing, cylindrical hydrogel samples with a diameter of 10 mm and a height of 10 mm were compressed at 1 mm min^{-1}. The test was stopped

© The National High School Journal of Science 2026



Scheme 1 Design, multifunctionality, and wound-healing application of Gel@CeO_2-TA hydrogel.

at 50% strain. Compressive strength was defined as the stress at 50% strain. The compressive modulus was calculated from the slope of the stress-strain curve within the initial linear region of 0-10% strain. All tests were performed with at least three replicates ($n \geq 3$).

Adhesion Performance

The adhesive properties of hydrogels were investigated using a universal mechanical testing machine 20 N loadcell. Both lap-shear and interfacial peel models were employed for testing. All adhesion tests were displacement-controlled at a fixed rate of 5 mm min^{-1}. Fresh porcine skin was purchased from a local supermarket. Visible surface fat was removed before testing. For the lap-shear model, sausage casing was bonded to transparent polyethylene terephthalate PET film using instant adhesive. A 300 µL precursor solution was dispensed onto a porcine skin surface 15mm×10mm, and the PET film with adhered casing was aligned and cured under UV light for 1 min. Lap-shear testing was then conducted to record the force-displacement curve and calculate adhesive strength. For the interfacial peel test, porcine skin was fixed horizontally on the testing platform. A 300 µL hydrogel precursor was applied to a defined bonding area and photocured under 405 nm light for 1 min. The free end of the bonded specimen was peeled from the skin surface at an angle of 90° using a universal mechanical tester. The peeling rate was set at 5 mm min^{-1}. The force-displacement curve was recorded during peeling. The interfacial toughness was calculated from the steady-state peeling force normalized by the specimen width. In addition, porcine skin was hydrated in saline, and dyed precursor solution was dripped onto the surface. Photo-crosslinking formed an in situ gel, which was subjected to bending, stretching, twisting, water immersion, and rinsing. Adhesion performance was visually documented via photography. All tests were performed with at least three replicates ($n \geq 3$).

Cytocompatibility

Direct contact co-culture of hydrogel with L929 mouse fibroblasts assessed cell viability and proliferation. Precursors and condensing reagents were UV-sterilized overnight. Cells were cultured in DMEM with 10% FBS, penicillin 1.0×10^5 UL^{-1}, and streptomycin 100 mgL^{-1}, with medium refreshed every 48 h. L929 cells 4,000cells/well were seeded on hydrogel surfaces in 96-well plates blank wells as control. After 1, 4, and 7 days in a 5% CO_2 incubator 37°C, viability was quantified via CCK-8 assay. After 24 h co-culture, stained cells were imaged via CLSM to visualize viability.

Antibacterial Assay

The antibacterial activity of different hydrogel groups was investigated using Escherichia coli Gram-negative and Staphy-

© The National High School Journal of Science 2026

lococcus aureus Gram−positive as test strains (All bacterial strains are sourced from BNCC). Bacterial suspensions were cultured in LB broth at 37°C for 24 h and diluted to 1×10^6 CFU mL^{-1}. Then, 100 mg of each hydrogel group was added to 200 μL of bacterial suspension and incubated at 37°C for 6 h. After incubation, 100 μL of the mixture was transferred to a 96-well plate, and the optical density (OD) at 600 nm was measured using a microplate reader. The mixed solution was diluted ($1:10^4$) with fresh LB medium. Subsequently, 100 μL of the diluted suspension was spread on agar plates and incubated at 37°C for 24 h before photographic documentation. CFU mL^{-1} was calculated as colony number × dilution factor / plated volume (mL). Antibacterial rate was calculated as $(CFU_{control} - CFU_{sample})/CFU_{control} \times 100\%$. The analysis was based on CFU counts rather than OD600, thereby avoiding optical interference from CeO_2, TA, or hydrogel fragments[25].

Antioxidant and Cellular ROS Assays

DPPH scavenging was measured using hydrogel extracts and component-matched blanks. Extracts from Gel, Gel@CeO_2, Gel@TA, and Gel@CeO_2-TA were incubated with DPPH in the dark, and absorbance at 517 nm was measured after 30 min. Scavenging was calculated as $(A_{control} - A_{sample})/A_{control} \times 100\%$ after blank correction. TMB hydroxyl-radical scavenging was evaluated using the TMB assay. Hydroxyl radicals were generated by the Fenton reaction. Briefly, 500 μL of 2 mM H_2O_2 was mixed with 500 μL of 2 mM $FeSO_4$. Hydrogel samples (25 mg) were immersed in 1 mL of the reaction solution and incubated at 37 °C for 30 min. After incubation, 100 μL of the supernatant was mixed with 100 μL of 10 mM TMB dissolved in DMSO. The mixture was incubated for 10 min, and the absorbance was measured at 650 nm. A Fenton reaction without hydrogel was used as the control. The hydroxyl-radical scavenging rate was calculated as $(A_{control} - A_{sample})/A_{control} \times 100\%$ after blank correction. H_2O_2 scavenging was determined using a potassium iodide colorimetric assay. Hydrogel samples (200 mg) were immersed in 1 mL of 0.8 mM H_2O_2 and incubated at 37 °C for 1.5 h. After incubation, 150 μL of the supernatant was mixed with 150 μL of 1 M KI. The mixture was incubated for 5 min, and the absorbance was measured at 350 nm. H_2O_2 solution without hydrogel was used as the control. The H_2O_2 scavenging rate was calculated as $(A_{control} - A_{sample})/A_{control} \times 100\%$ after blank correction[26].

Full-Thickness Wound Model and Histological staining

Male Sprague-Dawley (SD) rats aged 6-8 weeks were used to establish a superficial skin wound model. All rats were purchased from Shanghai Yishang Biotechnology Co., Ltd. The animal experiments were approved by the relevant ethics committee (approval no.: IACUC-2025-NI-086). The rats were randomly divided into four groups: Control, Gel, Gel@CeO_2-TA, and commercial dressing groups (n = 3 per group). The rats were anesthetized with 1% sodium pentobarbital. The dorsal hair was shaved and further removed using depilatory cream. A circular skin wound with a diameter of 12 mm was then created on the back using a scalpel. The Control group received no treatment. For the Gel and Gel@CeO_2-TA groups, 1 mL of the corresponding hydrogel precursor was applied to the wound. The precursor was then photocrosslinked for 1 min under UV irradiation. Wound healing was monitored and photographed on days 1, 3, 7, and 10. Skin samples were collected for histological analysis. The tissues were fixed, paraffin-embedded, and sectioned. Hematoxylin and eosin (H&E) staining and Masson's trichrome staining were performed to evaluate tissue regeneration and collagen deposition. CD86 and CD206 staining was used to assess the inflammatory response and macrophage polarization. After the experiment, the heart, liver, spleen, lung, and kidney were collected from the rats. The organs were fixed, paraffin-embedded, sectioned, and stained with H&E. Histological changes were examined to evaluate the potential systemic toxicity of the materials. All stained sections were imaged using a Pannoramic MIDI digital slide scanner.

Statistical Analysis

Data are presented as mean ± standard deviation (SD). All experiments were performed with at least three independent replicates ($n \geq 3$). For comparisons among multiple groups at a single time point, one-way ANOVA followed by Tukey's multiple-comparison test was used. For experiments involving both treatment and time, two-way ANOVA was used when the corresponding raw data were available. Statistical significance was set at $p < 0.05$. Significance levels are indicated as *$p < 0.05$, **$p < 0.01$, ***$p < 0.001$, and ****$p < 0.0001$.

Results

GelMA and CeO_2 Characterization

The ^1H NMR spectrum of GelMA showed new signals in the methacryloyl vinyl region at approximately 5.4-6.1 ppm, together with a methyl signal near 1.9 ppm (Figure 1B). These signals confirmed the successful methacrylation of gelatin. The main amide bands of gelatin were retained in the FTIR spectrum, further supporting the preservation of the gelatin backbone after modification (Figure 1C). The nanoscale structure of CeO_2 is important for its catalytic activity. Smaller ceria particles provide a larger accessible surface area and more redox-active sites. The Ce^{3+}/Ce^{4+} balance and oxygen-defect chemistry also play key roles in ROS regulation. TEM revealed nanoscale CeO_2 domains with limited aggregation, and

© The National High School Journal of Science 2026

Table 1 Statistical reporting of exact p values

Dataset	Planned/used analysis	Exact p values		
Elongation at break	One-way ANOVA + Tukey	Gel vs Gel@CeO_2	**	p=0.0092
		Gel vs Gel@TA	****	p<0.0001
		Gel vs Gel@CeO_2-TA	ns	p=0.8997
		Gel@CeO_2 vs Gel@TA	**	p=0.0016
		Gel@CeO_2 vs Gel@CeO_2-TA	**	p=0.0039
		Gel@TA vs Gel@CeO_2-TA	****	p<0.0001
Toughness	One-way ANOVA + Tukey	Gel vs Gel@CeO_2	ns	p=0.0529
		Gel vs Gel@TA	****	p<0.0001
		Gel vs Gel@CeO_2-TA	****	p<0.0001
		Gel@CeO_2 vs Gel@TA	***	p=0.0002
		Gel@CeO_2 vs Gel@CeO_2-TA	***	p=0.0005
		Gel@TA vs Gel@CeO_2-TA	ns	p=0.8688
Compressive modulus	One-way ANOVA + Tukey	Gel vs Gel@CeO_2	****	p<0.0001
		Gel vs Gel@TA	****	p<0.0001
		Gel vs Gel@CeO_2-TA	****	p<0.0001
		Gel@CeO_2 vs Gel@TA	*	p=0.0246
		Gel@CeO_2 vs Gel@CeO_2-TA	ns	p=0.0626
		Gel@TA vs Gel@CeO_2-TA	***	p=0.0007
Compressive strength	One-way ANOVA + Tukey	Gel vs Gel@CeO_2	ns	p=0.1209
		Gel vs Gel@TA	*	p=0.0297
		Gel vs Gel@CeO_2-TA	***	p=0.0002
		Gel@CeO_2 vs Gel@TA	ns	p=0.7541
		Gel@CeO_2 vs Gel@CeO_2-TA	**	p=0.0022
		Gel@TA vs Gel@CeO_2-TA	**	p=0.0075
Adhesive strength	One-way ANOVA + Tukey	Gel vs Gel@CeO_2	ns	p=0.9746
		Gel vs Gel@TA	***	p=0.0003
		Gel vs Gel@CeO_2-TA	***	p=0.0001
		Gel@CeO_2 vs Gel@TA	***	p=0.0005
		Gel@CeO_2 vs Gel@CeO_2-TA	***	p=0.0002
		Gel@TA vs Gel@CeO_2-TA	ns	p=0.7066
Interface toughness	One-way ANOVA + Tukey	Gel vs Gel@CeO_2	ns	p=0.146
		Gel vs Gel@TA	****	p<0.0001
		Gel vs Gel@CeO_2-TA	****	p<0.0001
		Gel@CeO_2 vs Gel@TA	****	p<0.0001
		Gel@CeO_2 vs Gel@CeO_2-TA	****	p<0.0001
		Gel@TA vs Gel@CeO_2-TA	***	p=0.0003
Cell viability	Two-way ANOVA	1d		
		Control vs Gel	ns	p=0.5637
		Control vs Gel@TA	ns	p=0.4652
		Control vs Gel@CeO_2-TA	ns	p=0.1607
		Control vs Gel@CeO_2	ns	p=0.2022
		4d		
		Control vs Gel	ns	p>0.9999
		Control vs Gel@TA	ns	p=0.9902
		Control vs Gel@CeO_2-TA	ns	p=0.7666
		Control vs Gel@CeO_2	ns	p=0.8418
		7d		
		Control vs Gel	ns	p=0.0613
		Control vs Gel@TA	*	p=0.0247
		Control vs Gel@CeO_2-TA	ns	p=0.1393
		Control vs Gel@CeO_2	ns	p=0.1684

Dataset	Planned/used analysis	Exact p values		
Antibacterial rate	One-way ANOVA + Tukey	Control vs Gel	ns	p=0.6219
		Control vs Gel@CeO_2	****	p<0.0001
		Control vs Gel@TA	****	p<0.0001
		Control vs Gel@CeO_2-TA	****	p<0.0001
		Gel vs Gel@CeO_2	****	p<0.0001
		Gel vs Gel@TA	****	p<0.0001
		Gel vs Gel@CeO_2-TA	****	p<0.0001
		Gel@CeO_2 vs Gel@TA	ns	p=0.1669
		Gel@CeO_2 vs Gel@CeO_2-TA	*	p=0.022
		Gel@TA vs Gel@CeO_2-TA	**	p=0.0031
DPPH· Scavenging ability	One-way ANOVA + Tukey	Control vs Gel	ns	p=0.9995
		Control vs Gel@CeO_2	****	p<0.0001
		Control vs Gel@TA	****	p<0.0001
		Control vs Gel@CeO_2-TA	****	p<0.0001
		Gel vs Gel@CeO_2	****	p<0.0001
		Gel vs Gel@TA	****	p<0.0001
		Gel vs Gel@CeO_2-TA	****	p<0.0001
		Gel@CeO_2 vs Gel@TA	ns	p=0.1204
		Gel@CeO_2 vs Gel@CeO_2-TA	***	p=0.0002
		Gel@TA vs Gel@CeO_2-TA	****	p<0.0001
OH· Scavenging ability	One-way ANOVA + Tukey	Control vs Gel	ns	p>0.9999
		Control vs Gel@CeO_2	****	p<0.0001
		Control vs Gel@TA	****	p<0.0001
		Control vs Gel@CeO_2-TA	****	p<0.0001
		Gel vs Gel@CeO_2	****	p<0.0001
		Gel vs Gel@TA	****	p<0.0001
		Gel vs Gel@CeO_2-TA	****	p<0.0001
		Gel@CeO_2 vs Gel@TA	ns	p=0.5660
		Gel@CeO_2 vs Gel@CeO_2-TA	**	p=0.0018
		Gel@TA vs Gel@CeO_2-TA	***	p=0.0003
H_2O_2 Scavenging ability	One-way ANOVA + Tukey	Control vs Gel	ns	p>0.9999
		Control vs Gel@CeO_2	****	p<0.0001
		Control vs Gel@TA	**	p=0.0074
		Control vs Gel@CeO_2-TA	****	p<0.0001
		Gel vs Gel@CeO_2	****	p<0.0001
		Gel vs Gel@TA	**	p=0.0089
		Gel vs Gel@CeO_2-TA	****	p<0.0001
		Gel@CeO_2 vs Gel@TA	****	p<0.0001
		Gel@CeO_2 vs Gel@CeO_2-TA	****	p<0.0001
		Gel@TA vs Gel@CeO_2-TA	****	p<0.0001
Wound length	One-way ANOVA + Tukey	Control vs Gel	*	p=0.0313
		Control vs Gel@CeO_2-TA	****	p<0.0001
		Control vs Dressing	**	p=0.0028
		Gel vs Gel@CeO_2-TA	**	p=0.0024
		Gel vs Dressing	ns	p=0.307
		Gel@CeO_2-TA vs Dressing	*	p=0.0254
CD206 positive area	One-way ANOVA + Tukey	Control vs Gel	**	p=0.001
		Control vs Gel@CeO_2-TA	****	p<0.0001
		Control vs Dressing	****	p<0.0001
		Gel vs Gel@CeO_2-TA	****	p<0.0001
		Gel vs Dressing	**	p=0.0022
		Gel@CeO_2-TA vs Dressing	***	p=0.001
CD86 positive area	One-way ANOVA + Tukey	Control vs Gel	***	p=0.0005
		Control vs Gel@CeO_2-TA	****	p<0.0001
		Control vs Dressing	****	p<0.0001
		Gel vs Gel@CeO_2-TA	****	p<0.0001
		Gel vs Dressing	ns	p=0.1071
		Gel@CeO_2-TA vs Dressing	****	p<0.0001

© The National High School Journal of Science 2026

elemental mapping showed a uniform distribution of Ce and O (Figure 1D). DLS showed a dominant hydrodynamic size of approximately 80-100 nm, with a zeta potential of about +20 mV (Figure 1E). XPS confirmed the presence of Ce and O, while Ce 3d spectra showed the coexistence of Ce^{3+} and Ce^{4+} states (Figure 1F,G). XRD displayed characteristic reflections at approximately 28.5°, 33.1°, 47.5°, 56.3°, 59.1°, 69.4°, and 76.7°, consistent with the fluorite structure of CeO_2 (Figure 1H). These results confirmed the successful preparation of nanoscale CeO_2 with mixed cerium valence states.

Hydrogel Gelation, Release, Degradation, and Morphology

Gel and Gel@CeO_2-TA formed stable hydrogels within 60 s under the selected 405 nm curing condition (Figure 1L). Frequency sweeps showed that storage behavior dominated across the tested range, confirming an elastic gel state (Figure 1K). The composite maintained an interconnected porous structure after freeze-drying (Figure 1M). The cumulative release profile increased progressively and approached approximately 95% by 48 h (Figure 1I). Degradation was formulation dependent (Figure 1J). By day 30, Gel retained only about 10% of its initial dry mass. Gel@CeO_2 retained approximately 25-30%, Gel@TA retained approximately 45%, and Gel@CeO_2-TA retained approximately 55%. The slower degradation of TA-containing samples is consistent with additional noncovalent interactions between polyphenol groups and GelMA chains, while the CeO_2-containing phase may provide additional physical reinforcement.

Mechanical and Tissue-Adhesive Properties

Adding CeO_2 or TA altered the mechanical response of GelMA (Figure 2). Gel showed an elongation at break of approximately 125% and a tensile toughness of approximately 27 kJ/m^{-3}. Gel@CeO_2 increased these values to about 139% and 32 kJ/m^{-3}, while Gel@TA reached approximately 154% elongation and 44 kJ/m^{-3} toughness. The combined Gel@CeO_2-TA formulation showed an elongation near 124% but retained a high toughness of approximately 42 kJ/m^{-3}. Thus, the composite did not maximize extensibility, but it preserved high energy absorption.

The largest improvement was observed in compression. The compressive modulus increased from approximately 43 kPa for Gel to about 94 kPa for Gel@CeO_2, 82 kPa for Gel@TA, and 103 kPa for Gel@CeO_2-TA. Compressive strength increased from approximately 63 kPa for Gel to 69, 73, and 86 kPa for Gel@CeO_2, Gel@TA, and Gel@CeO_2-TA, respectively. TA also contributed strongly to tissue adhesion. Adhesive strength was approximately 12 kPa for Gel and Gel@CeO_2, but about 15.5-16 kPa for Gel@TA and Gel@CeO_2-TA. Interfacial toughness increased from approximately 42 J/m^2 for Gel to approximately 52 J/m^2 for Gel@CeO_2, 88 J/m^2 for Gel@TA, and 114 J/m^2 for Gel@CeO_2-TA. The composite also remained attached to porcine skin during bending and stretching (Figure 2K). Overall, CeO_2 mainly enhanced mechanical reinforcement, while TA contributed strongly to tissue adhesion. Their combined incorporation produced a mechanically robust and adhesive hydrogel suitable for wound coverage.

Cytocompatibility and Antibacterial Activity

Live/Dead staining showed predominantly viable L929 cells in all hydrogel groups (Figure 3A). CCK-8 measurements increased from approximately 90-100% at day 1 to roughly 190-200% at day 4 and 260-270% at day 7, with no large separation among the four hydrogel formulations (Figure 3C). These data indicate that the added CeO_2 and TA did not suppress fibroblast proliferation at the tested formulation.

Colony assays demonstrated clear inhibition of both test strains (Figure 3B,D). Gel alone showed little antibacterial activity. Gel@CeO_2 and Gel@TA each reduced colony formation, while Gel@CeO_2-TA showed the strongest effect. The antibacterial rate of the combined formulation was approximately 95% against *S. aureus* and approximately 92% against *E. coli*. The corresponding single-component values were approximately 87% and 83% against *S. aureus* and approximately 84% and 79% against *E. coli* for Gel@CeO_2 and Gel@TA, respectively. These results indicate that both CeO_2 and TA contributed to antibacterial activity, and their combined incorporation further enhanced bacterial inhibition[27].

Antioxidant performance and mechanism

The antioxidant activity of the hydrogels was evaluated using DPPH, TMB, and H_2O_2 scavenging assays (Figure 4). Gel showed minimal scavenging activity. Gel@CeO_2 removed approximately 86% of DPPH radicals, 86% of hydroxyl radicals, and 78% of H_2O_2. Gel@TA showed approximately 82% scavenging of both DPPH and hydroxyl radicals, but only limited H_2O_2 removal. Gel@CeO_2-TA showed the strongest antioxidant activity in all three assays. Its scavenging rates reached approximately 95% for DPPH, 96% for hydroxyl radicals, and 95% for H_2O_2. Consistently, intracellular ROS fluorescence was lowest in the Gel@CeO_2-TA group (Figure 4D). These results indicate that CeO_2 and TA provide complementary antioxidant functions and enhance ROS scavenging when combined.

The antioxidant activity of CeO_2 is mainly associated with reversible Ce^{3+}/Ce^{4+} redox cycling and oxygen-vacancy-mediated surface reactions[15-17]. In CeO_2-TA metal-polyphenol systems, coordination between TA and cerium can

© The National High School Journal of Science 2026

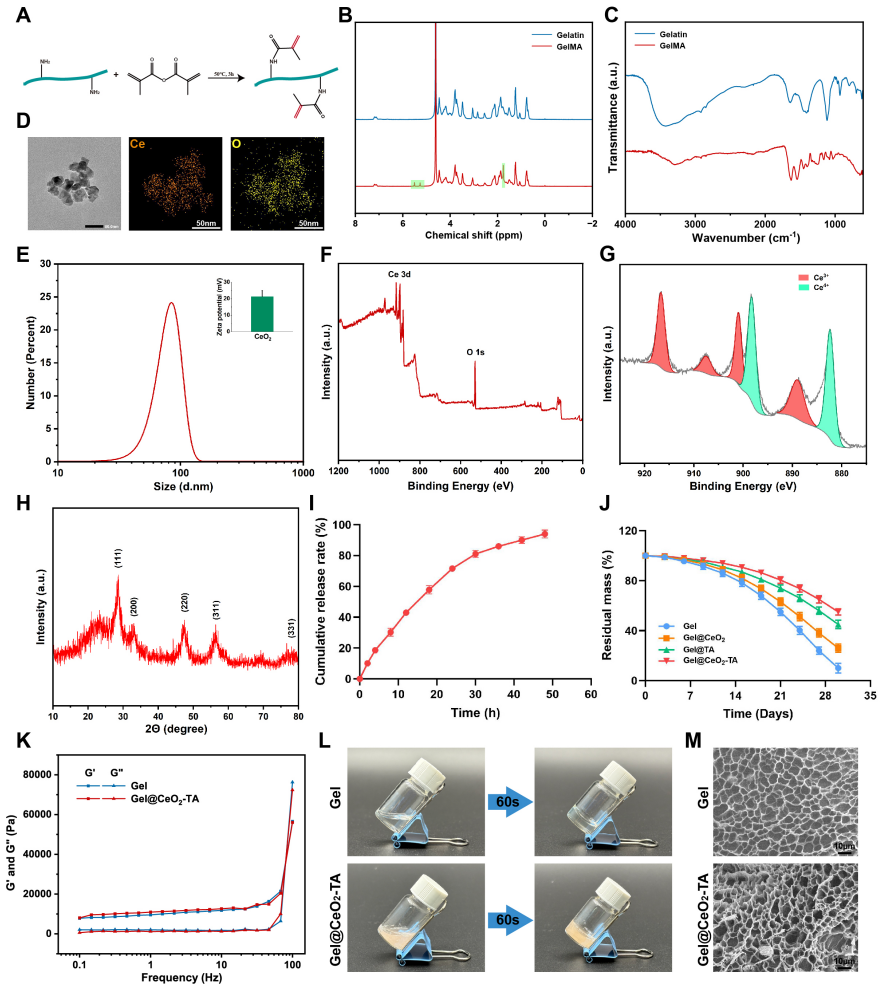


Figure. 1 Synthesis and physicochemical characterization. (A) GelMA methacrylation scheme. (B) ^{1}H NMR spectra of gelatin and GelMA. (C) FTIR spectra. (D) TEM image of CeO_2 and elemental mapping of Ce and O. (E) DLS size distribution with zeta-potential inset. (F) XPS survey spectrum. (G) Ce 3d peak deconvolution showing Ce^{3+}/Ce^{4+} contributions. (H) XRD pattern of CeO_2. (I) Cumulative release profile of the CeO_2-containing phase over 48 h. (J) Residual mass during 30 d degradation. (K) Frequency-sweep rheology of Gel and Gel@CeO_2-TA. (L) Vial-tilt gelation test at 60 s. (M) SEM images of freeze-dried Gel and Gel@CeO_2-TA. Data are mean ± SD where error bars are shown (n≥3).

further regulate surface electronic structure and oxygen vacancies, which may enhance ROS-scavenging activity[20]. TA-Ce nanoenzymes have also been reported to remove multiple ROS and reduce inflammatory signaling in vivo[22,24]. Based on these mechanisms, Figure 4E illustrates a proposed pathway for ROS regulation by Gel@CeO_2-TA.

In Vivo Wound Repair

The full-thickness wound model was used to evaluate the wound-healing performance of the hydrogels (Figure 5). All groups showed comparable wound areas on day 0. By day 3, the residual wound areas were approximately 95% for the Control group, 90% for Gel, 85% for the commercial dressing, and 78% for Gel@CeO_2-TA. By day 7, the corresponding values decreased to approximately 60%, 56%, 50%, and 42%, respectively. On day 10, Gel@CeO_2-TA showed the smallest residual wound area at approximately 22%. In comparison, the values were approximately 45% for the Control group, 35% for Gel, and 32% for the commercial dressing.

Wound length measurements showed a similar trend (Figure 5D). The mean wound length was approximately 6.6 mm in the Control group, 5.2 mm in the Gel group, 4.4 mm in the commercial dressing group, and 3.0 mm in the Gel@CeO_2-TA group. Histological analysis further confirmed improved tissue repair. H&E staining showed a more continuous epithe-

© The National High School Journal of Science 2026

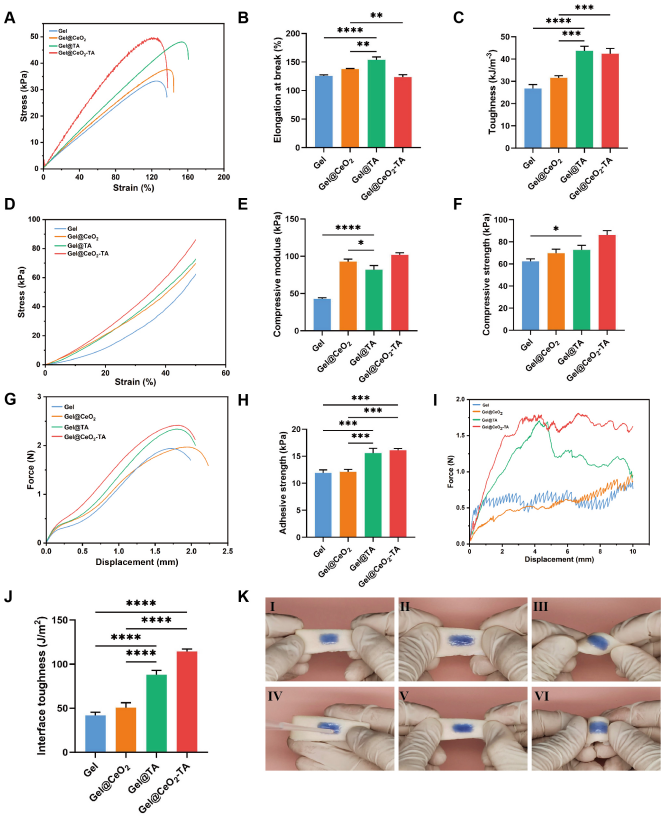


Figure. 2 Mechanical and tissue-adhesive properties of the four hydrogel formulations. (A) Tensile stress-strain curves. (B) Elongation at break. (C) Tensile toughness. (D) Compressive stress-strain curves. (E) Compressive modulus. (F) Compressive strength. (G) Lap-shear force-displacement curves. (H) Adhesive strength. (I) Interfacial peel force-displacement curves. (J) Interfacial toughness. (K) Representative photographs showing tissue adhesion during deformation. Significance symbols are reproduced from the provided statistical plots (n≥3).

lial layer in the Gel@CeO_2-TA group. Masson's trichrome staining showed denser and more organized collagen deposition in the regenerated tissue (Figure 5E). Together, these results indicate that Gel@CeO_2-TA accelerated wound closure and promoted tissue regeneration in the full-thickness wound model.

Histological staining

Immunofluorescence staining showed clear changes in macrophage polarization (Figure 6A-C). The CD86-positive area was approximately 68% in the Control group and 52% in the Gel group. Gel@CeO_2-TA reduced the CD86-positive area to approximately 2-3%, compared with about 45% in the commercial dressing group. In contrast, the CD206-positive area increased from approximately 7% in the Control group to 24% in the Gel group, 55% in the Gel@CeO_2-TA group, and 39% in the commercial dressing group. The decrease in CD86 and increase in CD206 indicate a shift from a pro-inflammatory M1-like phenotype toward a pro-repair M2-like phenotype.

H&E staining of the heart, liver, spleen, lung, and kidney showed no obvious structural abnormalities during the experimental period (Figure 6D). These results suggest good short-term histological biosafety of Gel@CeO_2-TA under the tested conditions.

Discussion

Structure-Property Relationships

CeO_2 and TA contributed differently to the mechanical behavior of the hydrogel. CeO_2 mainly enhanced compressive performance, whereas TA had a stronger effect on tensile extensibility, tissue adhesion, and interfacial toughness. Gel@CeO_2-TA showed the highest compressive modulus, compressive strength, adhesive strength, and interfacial toughness among the tested groups. However, its elongation at break was not the highest. These results suggest complementary rather than uniform reinforcement by CeO_2 and TA. TA contains abundant phenolic groups that can form hydrogen bonds and other noncovalent interactions with GelMA chains and tissue surfaces. CeO_2 provides an inorganic reinforcing phase that can restrict polymer-chain motion and increase resistance to compression. The combination of these effects improves the overall mechanical stability and tissue adhesion of the hydrogel.

ROS Regulation and Antibacterial Function

TA and CeO_2 showed distinct contributions to ROS scavenging. TA efficiently removed DPPH and hydroxyl radicals, while CeO_2 contributed more strongly to H_2O_2 removal. Gel@CeO_2-TA retained both activities and showed the highest overall ROS-scavenging capacity. This functional complementarity is consistent with metal-polyphenol systems, in which phenolic ligands directly quench free radicals and metal-based components provide redox-active catalytic sites[28]. The coexistence of Ce^{3+} and Ce^{4+} observed by XPS further supports reversible redox cycling in nanoceria.

A similar trend was observed in the antibacterial assays. Both Gel@CeO_2 and Gel@TA reduced colony formation of *S. aureus* and *E. coli*, while Gel@CeO_2-TA showed the strongest antibacterial activity. TA can disrupt bacterial membranes and interfere with protein function. CeO_2 may also affect bacterial redox balance and interact with the cell envelope. Their combined incorporation therefore provides multiple antibacterial mechanisms within the GelMA network.

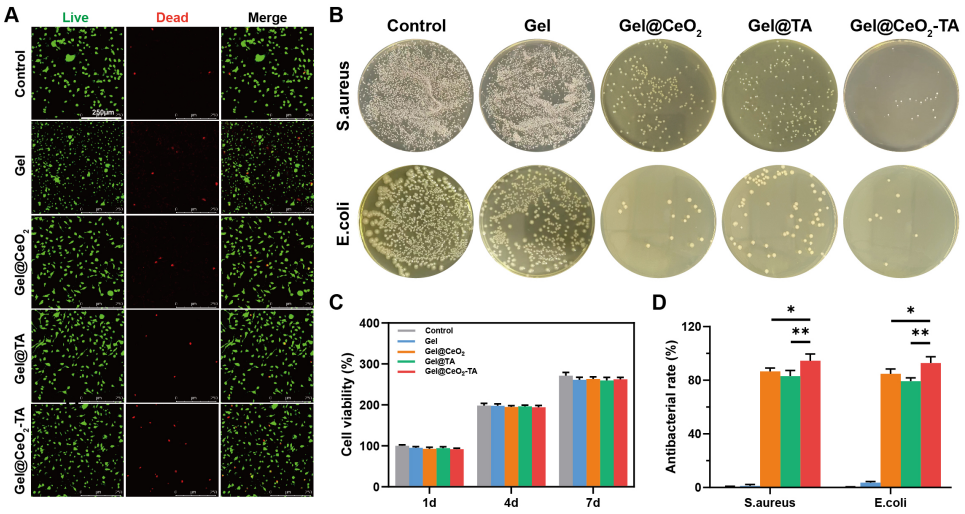


Figure. 3 Cytocompatibility and antibacterial performance. (A) Live/Dead staining of L929 fibroblasts for control, Gel, Gel@CeO_2, Gel@TA, and Gel@CeO_2-TA. (B) Representative colony plates for *S. aureus* and *E. coli* after treatment. (C) CCK-8 cell proliferation at days 1, 4, and 7. (D) antibacterial rates. Data are mean ± SD (n≥3).

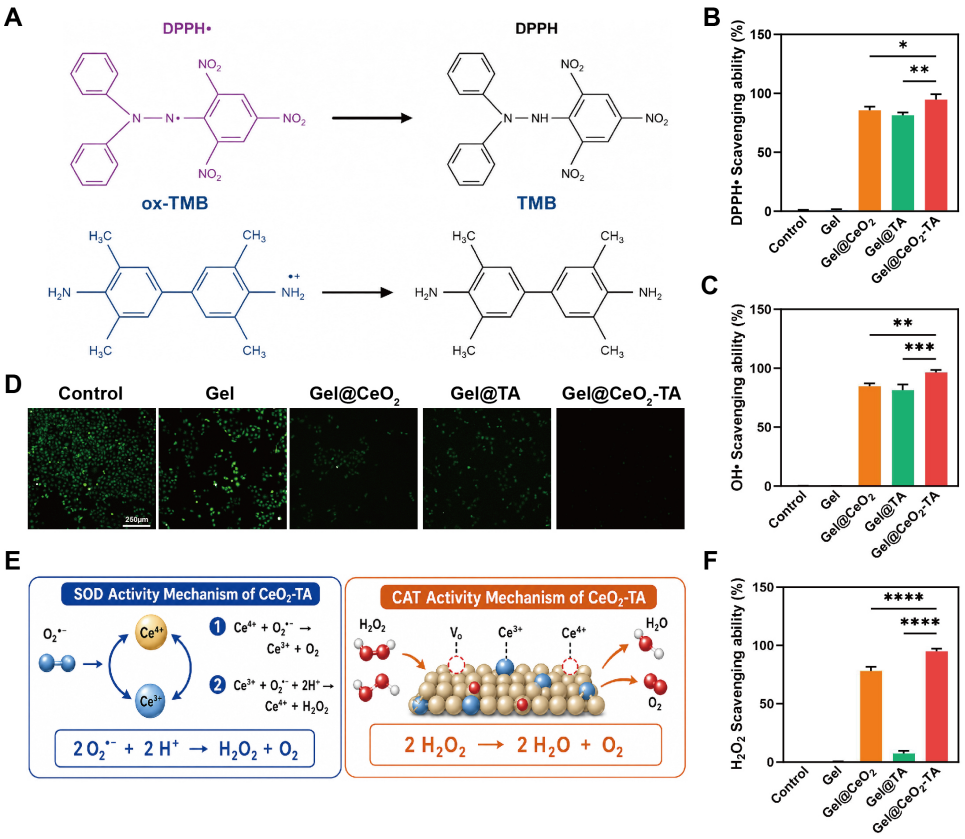


Figure. 4 Antioxidant activity. (A) Chemical structures illustrating DPPH• reduction to DPPH and ox-TMB reduction to TMB. (B) DPPH-scavenging ability. (C) Hydroxyl-radical-scavenging ability. (D) Representative intracellular ROS fluorescence images. (E) Mechanism of SOD-like and CAT-like enzyme activities of CeO_2-TA. (F) H_2O_2-scavenging ability. Data are mean ± SD (n≥3).

© The National High School Journal of Science 2026

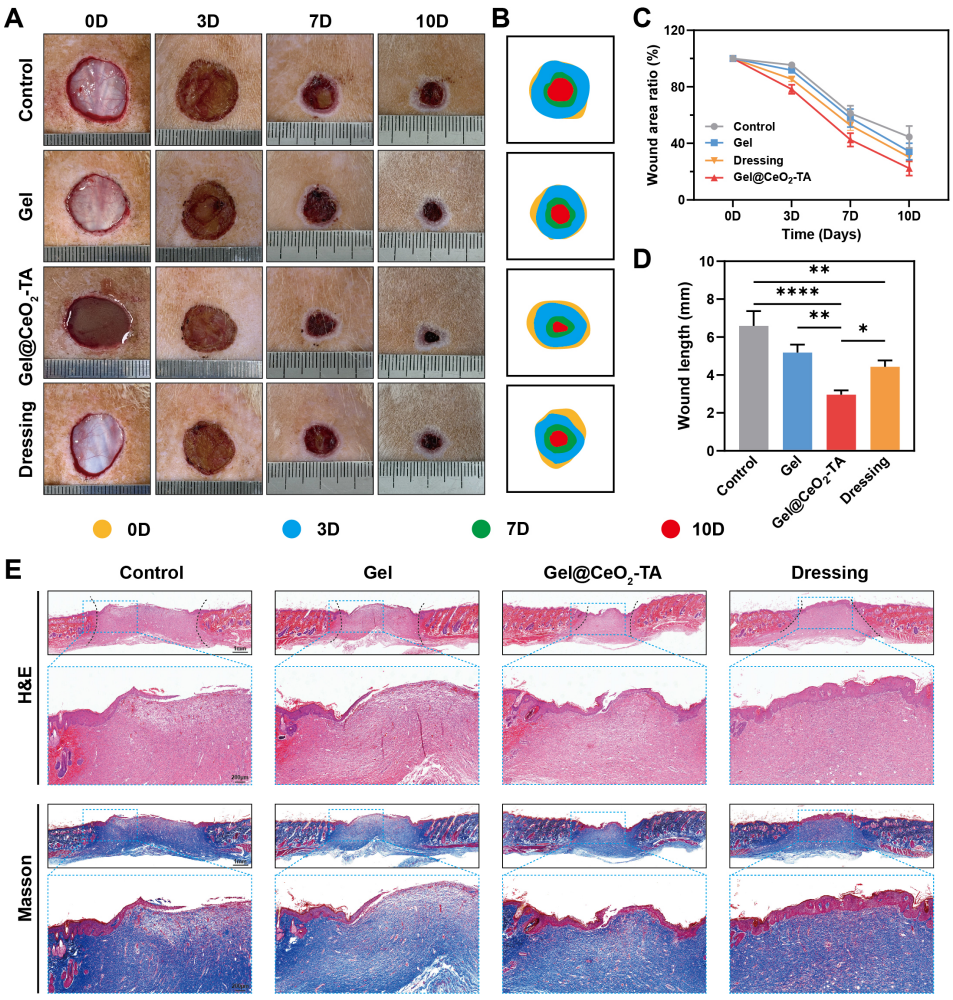


Figure. 5 Full-thickness wound-healing evaluation. (A) Representative wound photographs at days 0, 3, 7, and 10 for untreated control, Gel, Gel@CeO_2-TA, and a commercial dressing comparator. (B) Superimposed wound outlines. (C) Residual wound-area ratio over time. (D) Endpoint wound length. (E) H&E and Masson's trichrome staining at the endpoint, with enlarged views of the wound region. Data are mean ± SD (n=3).

Inflammation and Wound Repair

Gel@CeO_2-TA accelerated wound closure and improved tissue regeneration compared with Gel and the untreated control. The commercial dressing provided an additional benchmark. Gel@CeO_2-TA showed a smaller residual wound area and shorter wound length at day 10. H&E staining showed improved re-epithelialization, while Masson's trichrome staining showed denser and more organized collagen deposition. The improved repair may be related to the combined antioxidant, antibacterial, adhesive, and immunomodulatory properties of the hydrogel. Lower oxidative stress can reduce tissue damage and support cell survival. Stable tissue adhesion can also maintain close contact between the hydrogel and wound surface. Immunofluorescence staining further showed a marked decrease in CD86 and an increase in CD206 in the Gel@CeO_2-TA group. This pattern indicates a shift from a pro-inflammatory M1-like phenotype toward a pro-repair M2-like phenotype. Similar macrophage responses have been reported for ROS-regulating nanozymes and metal-polyphenol systems[29]. These findings suggest that Gel@CeO_2-TA can regulate both oxidative and inflammatory features of the wound microenvironment.

Limitations

This study has several limitations. First, the advantages of nanoscale CeO_2 are therefore supported by particle characterization and previous studies rather than by a direct nano-versus-bulk comparison in this system. Second, the antiox-

© The National High School Journal of Science 2026

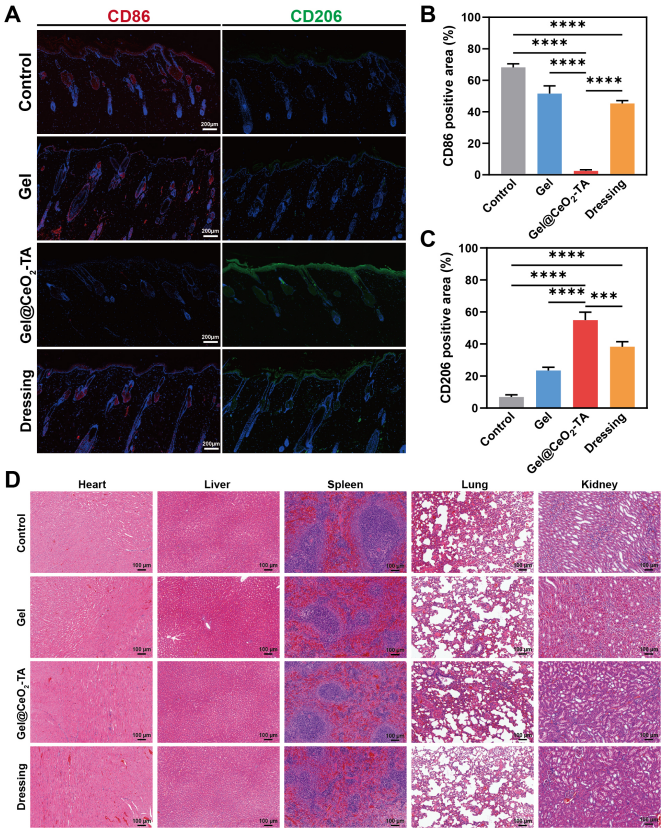


Figure. 6 Immunomodulatory response and major-organ histology. (A) Representative wound immunofluorescence for CD86 and CD206. (B) Quantified CD86-positive area. (C) Quantified CD206-positive area. (D) H&E staining of heart, liver, spleen, lung, and kidney. Data are mean ± SD (n=3).

idant assays demonstrated strong ROS scavenging, but detailed SOD- and CAT-like kinetic measurements were not performed. Third, H&E staining of major organs provides only short-term histological information. It cannot determine cerium biodistribution or long-term nanoparticle retention. Finally, the current full-thickness wound model does not reproduce the more complex microenvironment of infected or diabetic wounds. Future studies should evaluate the hydrogel in these disease-relevant models.

Conclusion

This study successfully developed a GelMA/CeO_2-TA composite hydrogel that combines mechanical reinforcement, tissue adhesion, antioxidant activity, antibacterial effects, and immunomodulatory behavior. CeO_2 and TA contributed distinct but complementary functions. The combined formulation showed high DPPH, TMB, and H_2O_2 scavenging, strong inhibition of *S. aureus* and *E. coli*, improved compressive and adhesive properties, and favorable fibroblast compatibility. In a full-thickness wound model, Gel@CeO_2-TA accelerated wound closure, improved re-epithelialization and collagen organization, reduced CD86-positive area, and increased CD206-positive area. These results support Gel@CeO_2-TA as a promising multifunctional wound-dressing platform for local microenvironment regulation and tissue repair.

Acknowledgements

I sincerely thank Dr. Liya Qi from Sinopec Beijing Research Institute of Chemical Industry (BRICI) for guidance throughout this work. I also thank Dan Pan and Lu Fan from Beijing 101 High School for their feedback and encouragement, and my family for their support during manuscript preparation.

References

1 Wei Q, Su J, Meng S, et al. MiR-17-5p-engineered sEVs Encapsulated in GelMA Hydrogel Facilitated Diabetic Wound Healing by Targeting PTEN and p21. Advanced Science. 2024;11:e2307761. https://doi.org/10.1002/advs.202307761.

2 Yang Y, Suo D, Xu T, et al. Sprayable Biomimetic Double Mask with Rapid Autophasing and Hierarchical Programming for Scarless Wound Healing. Science Advances. 2024;10:eado9479. https://doi.org/10.1126/sciadv.ado9479.

3 Xue Y, Yang F, He Y, et al. Multifunctional Hydrogel with Photothermal ROS Scavenging and Antibacterial Activity Accelerates Diabetic Wound Healing. Advanced Healthcare Materials. 2025;14:2402236. https://doi.org/10.1002/adhm.202402236.

4 Du J, Rybak D, Su Q, et al. Sprayable Photothermal Fiber-Embedded Hydrogels to Engineer Microenvironment for Infected Wound Healing. Advanced Functional Materials. 2025;2501242. https://doi.org/10.1002/adfm.202501242.

5 Wang H, Lyu C, Zhang C, et al. An Intelligent Hyperthermia System with Photothermal Temperature Wall Effect for Programmable Gated Drug Release in Wound Healing. Advanced Functional Materials. 2025;35:2422554. https://doi.org/10.1002/adfm.202422554.

6 He J, Sun Y, Gao Q, et al. Gelatin Methacryloyl Hydrogel, from Standardization, Performance, to Biomedical Application. Advanced Healthcare Materials. 2023;12:2300395. https://doi.org/10.1002/adhm.202300395.

7 Yuan X, Zhu Z, Xia P, et al. Tough Gelatin Hydrogel for Tissue Engineering. Advanced Science. 2023;10:2301665. https://doi.org/10.1002/advs.202301665.

8 Yi Y, Yang Z, Zhou C, et al. Quercetin-encapsulated GelMA Hydrogel Microneedle Reduces Oxidative Stress and Facilitates Wound Healing. Nano TransMed. 2024;3:100030. https://doi.org/10.1016/j.ntm.2024.100030.

9 Zhang Z, Zhang Y, Peng L, et al. Multifunctional Dual-layer Microneedles Loaded with Selenium-doped Carbon Quantum Dots and Astilbin for Ameliorating Diabetic Wound Healing. Materials Today Bio. 2025;32:101739. https://doi.org/10.1016/j.mtbio.2025.101739.

10 Zhang Y, Shi Z, Shu Y, et al. Cerium Nanozyme-Powered Hydrogel Microspheres Alleviate Thromboangiitis Obliterans via Enhanced Stem Cell Therapy. Small. 2025;21:2408748. https://doi.org/10.1002/smll.202408748.

© The National High School Journal of Science 2026

11 Xu Y, Luo Y, Weng Z, et al. Microenvironment-Responsive Metal-Phenolic Nanozyme Release Platform with Antibacterial, ROS Scavenging, and Osteogenesis for Periodontitis. ACS Nano. 2023;17:18732-18746. https://doi.org/10.1021/acsnano.3c01940.

12 Zhou C, Zhang L, Xu Z, Sun T, Gong M, Liu Y, Zhang D. Self-Propelled Ultrasmall AuNPs-Tannic Acid Hybrid Nanozyme with ROS-Scavenging and Anti-Inflammatory Activity for Drug-Induced Liver Injury Alleviation. Small. 2023;19:2206408. https://doi.org/10.1002/smll.202206408.

13 Wang J, Qiao L, Zhu G, Sun Q, Xie Y, Wang M, Xu Y, Li C. Biodegradable pyroptosis inducer with multienzyme-mimic activity kicks up reactive oxygen species storm for sensitizing immunotherapy. Journal of Controlled Release. 2024;370:438-452. https://doi.org/10.1016/j.jconrel.2024.04.054.

14 Deshpande S, Patil S, Kuchibhatla SVNT, Seal S. Size dependency variation in lattice parameter and valency states in nanocrystalline cerium oxide. Applied Physics Letters. 2005;87:133113. https://doi.org/10.1063/1.2061873.

15 Xue Y, Luan Q, Yang D, Yao X, Zhou K. Direct evidence for hydroxyl radical scavenging activity of cerium oxide nanoparticles. Journal of Physical Chemistry C. 2011;115:4433-4438. https://doi.org/10.1021/jp109819u.

16 Baldim V, Bedioui F, Mignet N, Margaill I, Berret JF. The enzyme-like catalytic activity of cerium oxide nanoparticles and its dependency on Ce3+ surface area concentration. Nanoscale. 2018;10:6971-6980. https://doi.org/10.1039/C8NR00325D.

17 Heckert EG, Karakoti AS, Seal S, Self WT. The role of cerium redox state in the SOD mimetic activity of nanoceria. Biomaterials. 2008;29:2705-2709. https://doi.org/10.1016/j.biomaterials.2008.03.014.

18 Xu X, Han Z, Li D, et al. Minocycline-Loaded Cerium Oxide Nanoparticles for the Enhanced Treatment of Intracerebral Hemorrhage. Advanced Functional Materials. 2024;34:2313198. https://doi.org/10.1002/adfm.202313198.

19 Chigurupati S, Mughal MR, Okun E, et al. Effects of cerium oxide nanoparticles on the growth of keratinocytes, fibroblasts and vascular endothelial cells in cutaneous wound healing. Biomaterials. 2013;34:2194-2201. https://doi.org/10.1016/j.biomaterials.2012.11.061.

20 Cui X, Han J, Li T, Liu W, Sun Q, Zhu F, Yang C, Fan D, Wei H. Metal-Polyphenol Network Confined Synthesis of Nanozymes with Programmable Oxygen Vacancies for UVB Photodamage Therapy. Nano Letters. 2026;26:7708-7718. https://doi.org/10.1021/acs.nanolett.6c01558.

21 Daré RG, Kolanthai E, Neal CJ, Fu Y, Seal S, Nakamura CV, Lautenschlager SOS. Cerium Oxide Nanoparticles Conjugated with Tannic Acid Prevent UVB-Induced Oxidative Stress in Fibroblasts: Evidence of a Promising Anti-Photodamage Agent. Antioxidants. 2023;12:190. https://doi.org/10.3390/antiox12010190.

22 Fu H, Wang Y, Huang B, Liang Z, Li Y, Cao Z, Wu J, Zhao Y. Tannic acid-cerium nanoenzymes serve as broad-spectrum antioxidants to alleviate acute kidney injury by modulating macrophage polarization, mitophagy and endoplasmic reticulum stress. Journal of Controlled Release. 2025;380:892-909. https://doi.org/10.1016/j.jconrel.2025.02.038.

23 Teng M, Li Z, Wu X, Zhang Z, Lu Z, Wu K, Guo J. Development of tannin-bridged cerium oxide microcubes-chitosan cryogel as a multifunctional wound dressing. Colloids and Surfaces B: Biointerfaces. 2022;214:112479. https://doi.org/10.1016/j.colsurfb.2022.112479.

24 He M, Zhang P, Bao S, Luo R, Chen L, Huang W, Jiang W, Zhang A. A DPEP1-Binding and mitochondria-targeted nanocomposite relieves acute respiratory distress syndrome by inhibiting Drp1-mediated mitochondria fission. Materials Today Bio. 2026;38:103291. https://doi.org/10.1016/j.mtbio.2026.103291.

25 Cao C, Yang N, Zhao Y, et al. Biodegradable Hydrogel with Thermo-response and Hemostatic Effect for Photothermal Enhanced Anti-infective Therapy. Nano Today. 2021;39:101165. https://doi.org/10.1016/j.nantod.2021.101165.

26 Tian S, Mei J, Zhang L, et al. Multifunctional Hydrogel Microneedle Patches Modulating Oxi-inflamm-aging for Diabetic Wound Healing. Small. 2024;20:2407340. https://doi.org/10.1002/smll.202407340.

27 Kuang Y, He X, Zhang Z, et al. Comparison study on the antibacterial activity of nano- or bulk-cerium oxide. Journal of Nanoscience and Nanotechnology. 2011;11:4103-4108. https://doi.org/10.1166/jnn.2011.3858.

28 Ge L, Ling J, Cao G, Ouyang XK, Wang N. Nanozyme doped chitosan hydrogel driven by glucose oxidase for dual regulation of ROS homeostasis and macrophage reprogramming in diabetic wound healing. Carbohydrate Polymers. 2026;373:124534. https://doi.org/10.1016/j.carbpol.2025.124534.

29 Rao X, Niu Y, Zhang Q, et al. Microenvironment-responsive Immunoregulatory Hydrogel Exerts Multi-regulation and Synergistic Reprogramming of Macrophages to Promote Diabetic Wound Healing. Chemical Engineering Journal. 2025;522:167896. https://doi.org/10.1016/j.cej.2025.167896.

© The National High School Journal of Science 2026